Multi-Frame Blind Deconvolution of Closely Spaced Dim Stellar Objects

Ronald M. Aung, Maj, USAF
Air Force Institute of Technology, Wright-Patterson AFB, OH 45433
Stephen C. Cain, Ph.D.
Air Force Institute of Technology, Wright-Patterson AFB, OH 45433

ABSTRACT

The estimation of the point spread function plays a critical role to overcome the Earth's turbulent atmosphere. This paper introduces blind deconvolution techniques to recover true undistorted astronomical images through the point spread function estimation. A novel two-step iterative blind deconvolution technique is proposed, for processing short exposure images, to detect and resolve a dim star in close proximity to a brighter one. We compare the performance of the new algorithm using two performance metrics, which are the ability to detect the dim star and the resolution between the dim star and bright star. In addition, a method for estimating the long exposure point spread function that results from the application of an adaptive optics system is introduced for use in future research.

Keywords: Imaging through Turbulence, Image Restoration, Dim Object Detection, Closely Spaced Objects

1. INTRODUCTION

Astronomical images are subject to many sources of degradation. Some of them are deterministic, such as the manufacturing defects in the optical systems. Some are predictable, such as the photon counting noise introduced by the charge-coupled devices (CCD) [1]. The degradation of interest in this paper is caused by the Earth's turbulent atmosphere, which is random and unpredictable. All these affects are manifested in the point spread function (PSF), which is a convolution between the true undistorted object function and a point spread invariant distortion [2]. There are two broad categories to overcome the negative effects of the atmospheric turbulence. They are short exposure and long exposure imaging. In this paper, we introduce the techniques for both. For the short exposure imaging, a mathematical model as well as computer simulated results are presented. For the long exposure imaging, a mathematical model is presented.

The estimation of the PSF for short exposure imaging is a distinctly different process than the approach used for estimating long exposure PSFs. Unlike long exposure images, short exposure images retain diffraction-limited information [3]. The image degradations are caused by fixed patterns of refractive index perturbations drifting across the imaging path under the influence of atmospheric turbulence [4]. To overcome the turbulence, we describe a two-step iterative blind deconvolution approach for multi-frame astronomical images, with the assumption that the atmospheric effects are uncorrelated between images. The first step is based on the multi-frame blind deconvolution proposed by Schulz [3], with the Gerchberg-Saxton phase retrieval implementation [5]. The estimates of the object function and the PSFs from the first step are further processed with the new algorithm in the second step. The new algorithm is also based on the expectation-maximization (EM) algorithm [6], similar to Schulz's approach. Using computer generated datasets, the performance of the new algorithm from the second step is compared with that of the baseline algorithm from the first step. The performance metrics are measured in terms of the ability to detect the dim star as well as the ability to resolve the dim star from the bright star.

This paper is organized as follows. In Section 2, the mathematical models for each step of the new two-step blind deconvolution approach are described. Then, it explains about the datasets and the Zernike polynomial based atmospheric wavefront generation. The section also compares the performance of the first step with that of the second step, using two performance metrics. Next, in Section 3, the mathematical model for estimating the long exposure PSF is described for future research. This paper is summarized in Section 4.

2. SHORT EXPOSURE IMAGING

In this section, a two-step iterative blind deconvolution algorithm for short exposure imaging is introduced, with the overall purpose of being able to detect and resolve a dim star in close proximity to a bright one. The first step is primarily used in estimating the bright star in the object function and the PSFs. Using the estimations from the first step, the second step detects and resolves the dim star which is in close proximity to the bright star.

2.1. Step 1: Locating the Bright Star

Since the first step is based on the work by Schulz [3], we used the symbols and notations that are consistent with Schulz's work. In this section, two dimensional (2D) coordinates are described with single variables.

2.1.1. Mathematical Model

We begin by defining the true undistorted object function, $\{o(x) : x \in X\}$, where X is the discretized 2D region over which the star intensities are defined. The object function then passes through some unknown random atmospheric PSFs, $\{h_k(y ; x) : x \in X, y \in Y, k = 1...K\}$, to form the image functions, $i_k(y)$, where Y is the discretized 2D region over which the image function is defined and K is the total number of PSFs.

$$i_k(y) = \sum_{x \in X} h_k(y - x) o(x) . \tag{1}$$

The PSF for diffraction-limited incoherent imaging is modeled as shown in the following equation [7].

$$h_k(x) = \left| \mathcal{F}\left[A(u) e^{j\theta(u)} \right] \right|^2 . \tag{2}$$

In this equation, A is the aperture function, θ is the phase function, u is the discretized 2D region over which the aperture and phase functions are defined, $\mathcal{F}$ is the Fourier transform, and j is the imaginary number. We also constrain the sum of the PSF to be one to ensure that the process is conservative. The phase, θ, is the atmospheric path delay of the light that enters the aperture at position u in the pupil plane. In this model, it is assumed that the atmospheric PSF can be modeled with phase aberrations utilizing the Zernike polynomials.

$$\theta(u) = \sum_{k=1}^{\infty} \alpha_k Z_k(u) , \tag{3}$$

where α_k represents the Zernike coefficients and Z_k are the Zernike polynomials. Upon arriving at the detector such as the CCD, the image functions are converted into the data functions, $d_k(y)$. The detector introduces the photon counting noise where the data functions assume the Poisson distributions with their means equivalent to the image functions as shown in the equation below.

$$\mathrm{E}\left[d_k(y) \right] = i_k(y) . \tag{4}$$

With the knowledge of the type of distribution along with the mean, the conditional expectation of the log-likelihood function of the unobserved functions of interest, h_k and o, given the observed function, d_k, is calculated. This step is called the expectation step (E-Step) of the expectation maximization (EM) algorithm, which was first proposed by Dempster, Laird, and Rubin [6]. In the second step known as the maximization step (M-Step), the conditional expectation is maximized with respect to the unobserved functions. The estimates for the object function and the PSF are given by Schulz as the followings:

$$o^{new}(x) = \frac{o^{old}(x)}{K} \sum_{\forall k} \sum_{\forall y} \frac{h_k^{old}(y - x) d_k(y)}{i_k^{old}(y)} , \tag{5}$$

$$h_k^{EM}(x) = h_k^{old}(x)\sum_{\forall y}\frac{o^{old}(y-x)d_k(y)}{i_k^{old}(y)}. \tag{6}$$

To further improve the performance, a phase retrieval algorithm is applied to the PSFs estimated from the EM algorithm, h_k^{EM}. In this paper, the iterative Gerchberg-Saxton phase retrieval algorithm [5] is used for its simplicity in the implementation.

$$h_k^{new}(x) = \text{PhaseRetrieve}\left[h_k^{EM}(x)\right]. \tag{7}$$

Therefore, each iteration of the blind deconvolution algorithm is made up of Equations (5), (6), and (7). A system level diagram is shown in Fig. 1. In this paper, Schulz's implementation of the EM algorithm with the Gerchberg-Saxton phase retrieval algorithm is simply called the baseline algorithm.

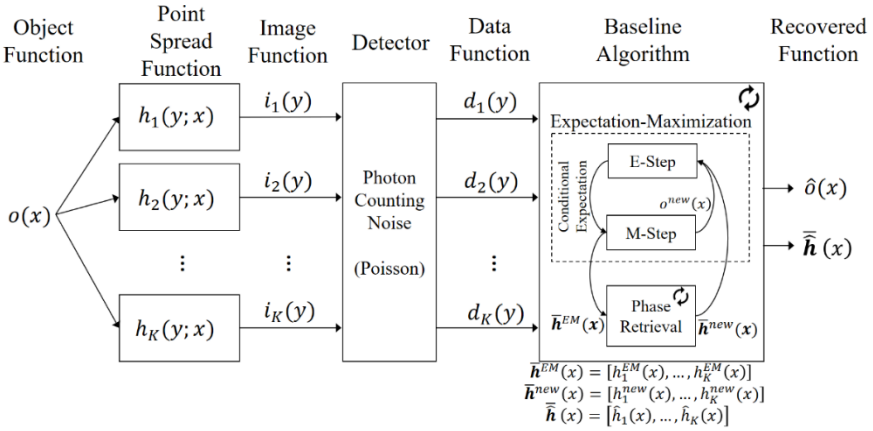

Fig. 1. System Level Diagram of the Baseline Algorithm.

2.1.2. Dataset Generation

The baseline algorithm is verified and validated with computer simulated data. All implementations are completed in the MATLAB programming language on a standard desktop computer. The MATLAB built-in functions are used throughout this paper.

2.1.3. Object Function

The object function is created with a 64×64 pixel plane to simulate a true undistorted astronomical image. A bright star is placed in the center at (32, 32) and a dim star is placed one pixel apart at (32, 34) as shown in Fig. 2. The intensity of the bright star is set to 10,000 photoelectrons while the intensities of the dim star are varied from 1,000 to 25 photoelectrons. A background intensity of 10 photoelectrons is added to every pixel. The scenarios used in this paper are summarized in Table 1.

Table 1. Scenarios for the Object Function.

Scenarios	Bright Star	Dim Star	Background
Scenario 1	10,000	1,000	10
Scenario 2	10,000	500	10
Scenario 3	10,000	250	10
Scenario 4	10,000	125	10
Scenario 5	10,000	100	10
Scenario 6	10,000	75	10
Scenario 7	10,000	50	10
Scenario 8	10,000	25	10

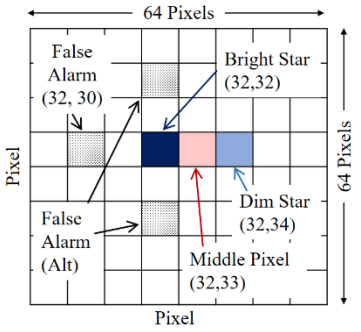

Fig. 2. Object Function.

2.1.4. Atmospheric Point Spread Function

The object function then passes through a set of random atmospheric PSFs to simulate turbulence. Even though there are many techniques to simulate turbulence, the Zernike polynomial based technique is used because it addresses the lower-order aberrations such as tilt, which makes up a majority of the atmospheric energy spectrum [8]. The technique used in this paper was proposed by Roddier [9] and implemented by Putnam and Cain [10].

The Zernike polynomials are a set of polynomials defined on a unit circle, with a key property of being orthogonal over the unit circle. A random wavefront, θ, is made up of a combination of Zernike polynomials, Z_i, scaled by the corresponding Zernike coefficients, a_i, as shown in Equation (3). The atmospheric coefficient correlation matrix, **C**, can be computed as the following:

$$\mathbf{C} = \mathrm{E}\left[\mathbf{A}\mathbf{A}^T\right], \tag{8}$$

where **A** is the Zernike coefficient vector. From the numerical analysis by Roddier, **C** is known to be Hermitian. Therefore, there exists a unitary matrix **U**, ($\mathbf{U}^{-1} = \mathbf{U}^T$), such that:

$$\mathbf{U}\mathbf{C}\mathbf{U}^T = \mathbf{D}, \tag{9}$$

where **D** is a diagonal matrix. Even though the Zernike polynomials are orthogonal over a unit circle, the Zernike coefficients are not statistically independent. To generate the Zernike coefficients from a set of independent and identically distributed (IID) random variables, an orthonormal basis is formed with the Karhunen-Loève functions.

$$\mathbf{N} = \mathbf{U}\mathbf{A}. \tag{10}$$

When the coefficients of **N** are made up of IID random variables from the zero mean, unit variance Gaussian distribution, **U** becomes the Cholesky decomposition of the correlation matrix, **C**.

$$\mathbf{U}\mathbf{C}\mathbf{U}^T = \mathbf{U}\left(\mathrm{E}\left[\mathbf{A}\mathbf{A}^T\right]\right)\mathbf{U}^T = \mathrm{E}\left[\mathbf{U}\mathbf{A}\mathbf{A}^T\mathbf{U}^T\right] = \mathrm{E}\left[\mathbf{N}\mathbf{N}^T\right] = \mathbf{I}. \tag{11}$$

Therefore, the Zernike coefficient vector can be generated with a set of zero mean, unit variance IID Gaussian random variables as the following equation.

$$\mathbf{A} = \mathbf{U}^T\mathbf{N}. \tag{12}$$

To generate random atmospheric PSFs, a turbulence-free PSF is first created with an aperture function that has a 32 pixel diameter pupil on a 64×64 pixel plane. The resultant turbulence-free PSF, h, is shown in Fig. 3 (a). Then, a set of five random atmospheric wavefronts are generated for each dataset with 100 Zernike coefficients, using Equations (2) and (3). The ratio between the aperture diameter and the seeing parameter is set to be two ($D/r_0 = 2$). Fig. 3 (b) through (f) show a set of five atmospheric PSFs. For each PSF, a random realization of the atmospheric wavefront is

used. Therefore, in this paper, no two wavefronts are the same, within any datasets or within any scenarios. We also make the assumption that no two wavefronts are correlated.

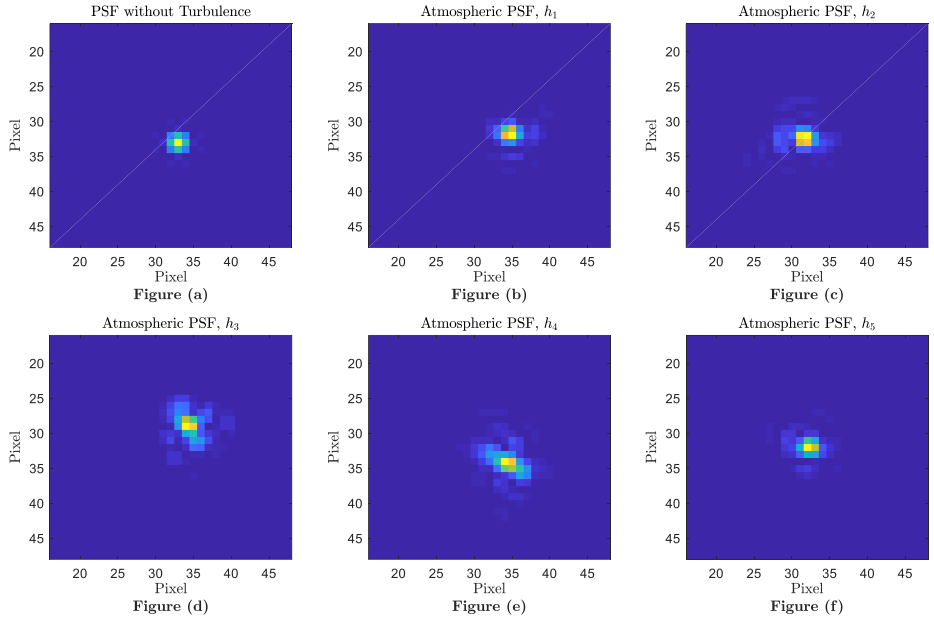

Fig. 3. A turbulence-free PSF and a set of five random atmospheric PSFs generated with the Zernike polynomial technique.

2.1.5. Image and Data Functions

As shown in Fig. 1, a set of five image functions are formed when an object function passes through a set of five atmospheric PSFs. When the image functions arrive at the detector, the detector coverts them into the data functions, by adding the photon counting noise. For each scenario described in Table 1, a total of 500 datasets are generated, with each dataset containing five data functions. Therefore, for each scenario, the 500 datasets are processed with the baseline algorithm to obtain the corresponding 500 recovered object functions as well as 500 sets of atmospheric PSFs, with each set containing five recovered PSFs.

2.1.6. Performance Metrics

To measure the performance, two metrics are used in this paper. The first one is the ability to detect the dim star by comparing between the intensities of the dim star and that of the false alarm location. The second is the resolution between the bright star and the dim star.

The first metric is calculated by means of the receiver operating characteristic (ROC) functions. For each scenario, the intensities of the dim star from the n^{th} dataset, $\{[\hat{\imath}_{det}]_n,\ n = 1\ldots500\}$ and that of the pixel at the false alarm location from the same dataset, $\{[\hat{\imath}_{fa}]_n,\ n = 1\ldots500\}$ are calculated using a correlation method with a 2D Gaussian mask function with a 0.5 pixel standard deviation in both horizontal and vertical directions. The Gaussian mask function is centered at the locations of the dim star and the false alarm pixel to calculate the intensities of the dim star and the false alarm pixels as shown in the equations below.

$$\left[\hat{i}_{det}\right]_n = \sum_{\forall x \in X}\left(\left[\hat{o}(x)\right]_n \times \frac{1}{2\pi\sigma^2}\exp\left(-\frac{\left(x-x_{det}\right)^T\left(x-x_{det}\right)}{2\sigma^2}\right)\right), \tag{13}$$

$$\left[\hat{i}_{fa}\right]_n = \sum_{\forall x \in X}\left(\left[\hat{o}(x)\right]_n \times \frac{1}{2\pi\sigma^2}\exp\left(-\frac{\left(x-x_{fa}\right)^T\left(x-x_{fa}\right)}{2\sigma^2}\right)\right), \tag{14}$$

where $[\hat{o}(x)]_n$ is the recovered object function from the n^{th} dataset, x_{det} and x_{fa} are the locations for the dim star and the false alarm pixel respectively, σ is the standard deviation of the Gaussian mask function in both horizontal and vertical directions, and × represents a pixel-by-pixel multiplication between two functions. As shown in Fig. 2, x_{det} and x_{fa} are located at (32, 34) and (32, 30) respectively. The intensities from the dim star and the false alarm location are then fitted to the gamma functions by estimating their shape and scale parameters [11]. These gamma fits are used in generating the ROC functions. As examples, Figures 5 and 6 show the probability distribution functions (PDF) and the cumulative distribution functions (CDF) for the intensities of the dim star and that of the false alarm location for Scenarios 3 and 6 respectively. Also shown in the figures are their gamma fits.

The second metric is the resolution between the bright star and the dim star. In this paper, the resolution function for each scenario, $\hat{o}_{res}(x)$, is obtained by calculating the mean of all 500 recovered object functions for that scenario as shown in the equation below.

$$\hat{o}_{res}(x) = \frac{1}{500}\sum_{n=1}^{500}\left[\hat{o}(x)\right]_n . \tag{15}$$

From the resolution function, the intensity of the middle pixel at (32, 33) is compared with that of the dim star at (32, 34). If the intensity of the middle pixel is less than that of the dim star, then the scenario is considered resolvable. Otherwise, the scenario is considered unresolvable.

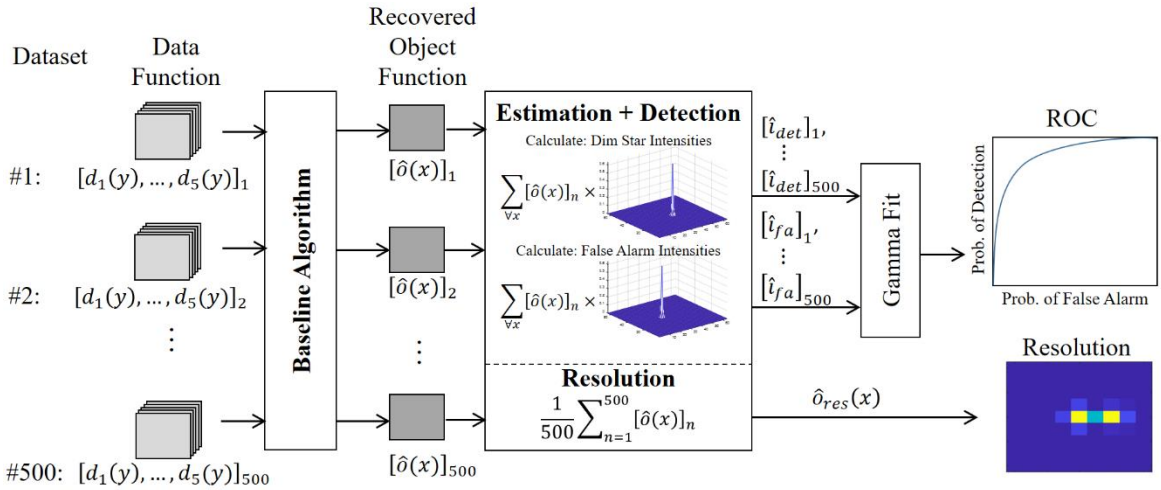

Fig. 4. The systems diagram for calculating the two performance metrics.

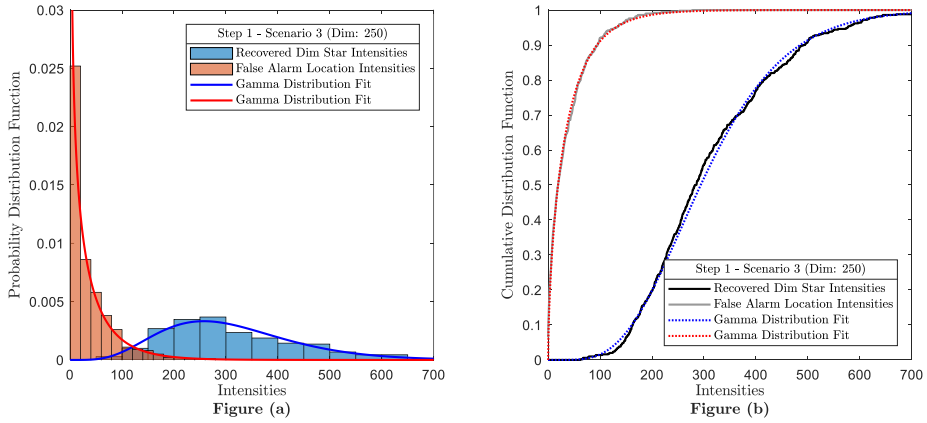

Fig. 5. The distributions of the intensities of the dim star and the false alarm pixel for Scenario 3.

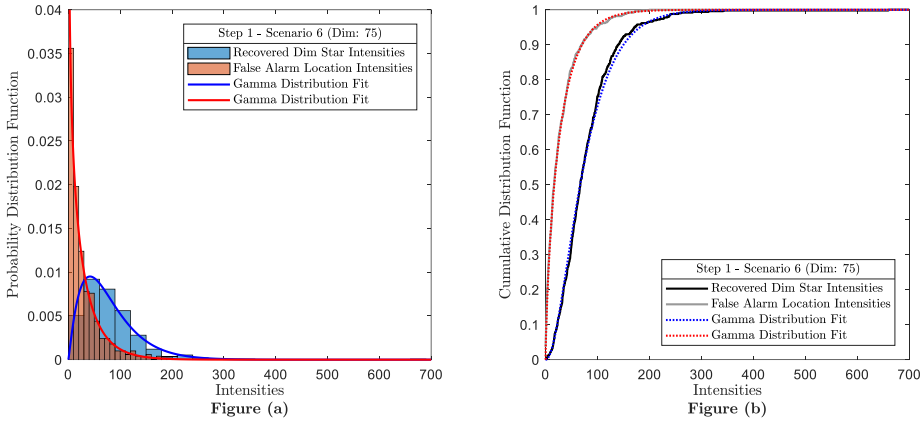

Fig. 6. The distributions of the intensities of the dim star and the false alarm pixel for Scenario 6.

2.1.7. Performance of Step 1

For the baseline algorithm, all scenarios are processed with 1,000 EM iterations. For any EM iteration performed in this paper, 100 phase retrieval iterations are always performed to recover the phase.

For the first performance metric, Fig. 7 shows the baseline algorithm's ability to detect the dim star by comparing the intensities of the dim star with that of the false alarm pixel for each scenario. From the result, the baseline algorithm has a perfect detection for Scenario 1 and a near-perfect detection for Scenario 2. However, as the intensity of the dim star is reduced, the performance also degrades. Even when the additional EM iterations are performed, the performance does not improve. Fig. 7 also shows the performance comparison between processing with 1,000 and 2,000 EM iterations.

For the second performance metric, Table 2 compares the intensity of the dim star with that of the middle pixel of the resolution function for each scenario. From the result, Scenario 1 is the only resolvable scenario, where the intensity of the dim star is higher than that of the middle pixel. Fig. 8 also shows the resolution functions for all scenarios.

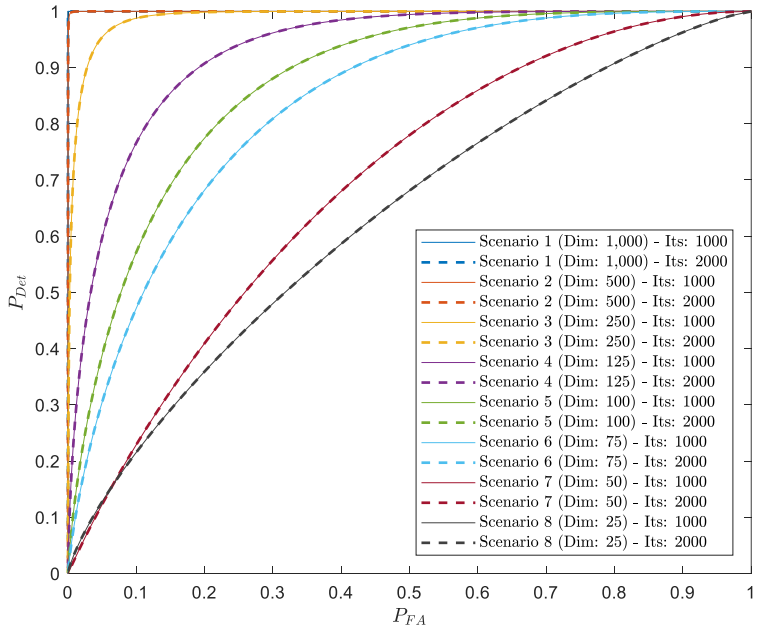

Fig. 7. The intensities of the dim star and the false alarm pixel are compared using the ROC functions.

Table 2. The comparison between the intensities of the dim star and the middle pixel of the resolution function for each scenario.

Scenarios	Middle Pixel at (32, 33)	Dim Star at (32, 34)	Resolvable
Scenario 1	691	1475	Yes
Scenario 2	652	590	No
Scenario 3	530	214	No
Scenario 4	404	79	No
Scenario 5	352	51	No
Scenario 6	261	31	No
Scenario 7	198	18	No
Scenario 8	177	10	No

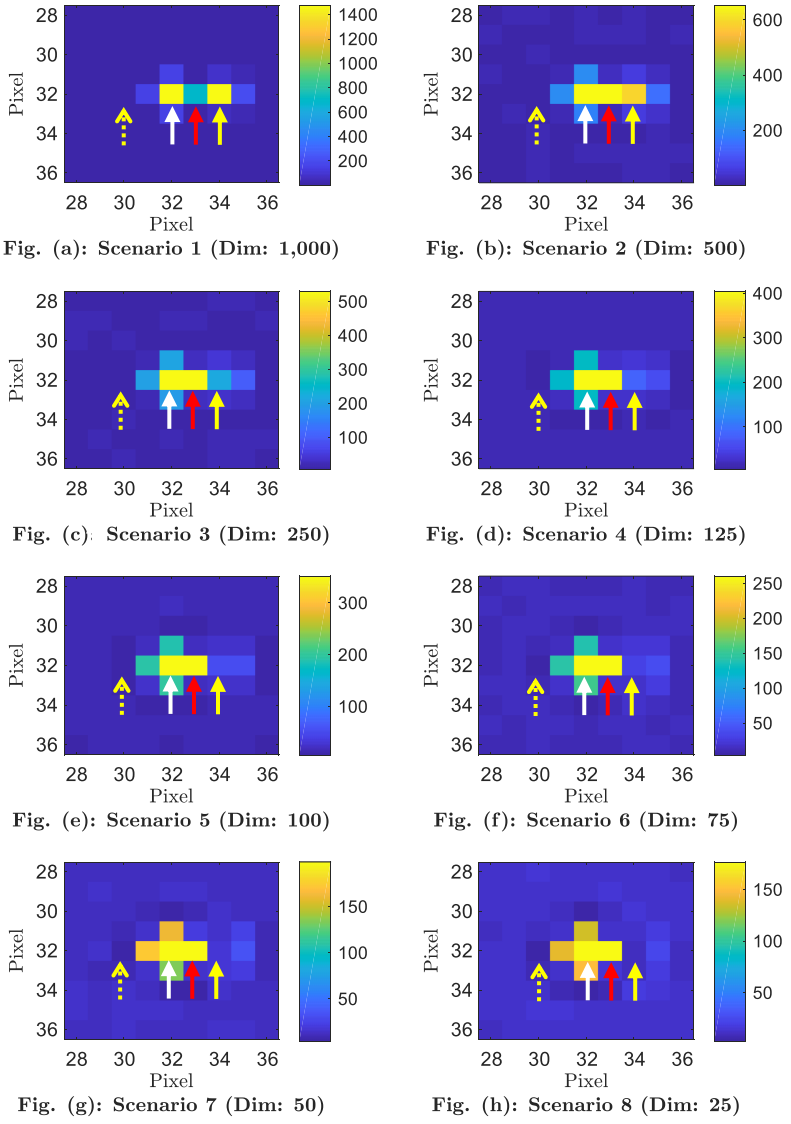

Fig. (a): Scenario 1 (Dim: 1,000)

Fig. (b): Scenario 2 (Dim: 500)

Fig. (c): Scenario 3 (Dim: 250)

Fig. (d): Scenario 4 (Dim: 125)

Fig. (e): Scenario 5 (Dim: 100)

Fig. (f): Scenario 6 (Dim: 75)

Fig. (g): Scenario 7 (Dim: 50)

Fig. (h): Scenario 8 (Dim: 25)

Fig. 8. The resolution functions are calculated by averaging all 500 recovered object functions each scenario, using the baseline algorithm. The solid white, red, and yellow arrows indicate the bright star, the middle pixel, and the dim star respectively. The dotted yellow arrow indicates the false alarm pixel. The intensities of the middle pixel and the dim star are summarized in Table 2. Note: the intensities of the bright star are matched to the second brightest pixel to reduce the contrast ratio for all scenarios.

2.2. Step 2: Detecting the Dim Star

Since the performance of the baseline algorithm saturates after 1,000 iterations, a new algorithm is introduced in this section to detect the dim star in close proximity to the bright one. This algorithm is adopted from the method proposed by Cain [12].

2.2.1. Mathematical Model

The new algorithm separates the object function into three sets, which are the primary bright star, $o_p(x)$, the unknown neighborhood system function around the bright star, $o_s(x)$, and the background light and dark current measured during the acquisition process, B.

$$o_p(x) = \gamma\delta(x - x_p), \tag{16}$$

$$o_s(x) = \sum_{m=1}^{M} \mu_m \delta(x - x_m), \tag{17}$$

$$o_b(x) = B, \tag{18}$$

where x_p and γ are the location and the magnitude of the bright star estimated from the baseline algorithm, μ_m is the number of photoelectrons emitted from the m^{th} star in the system, M is the total number of stars in the system, and δ is the Dirac Delta function. Applying the EM algorithm, similar to the approach used by Schulz, the update functions are derived as the following.

$$\gamma^{new} = \frac{\gamma^{old}}{K} \sum_{\forall k} \sum_{\forall y} \frac{h_k^{old}(y - x_p) d_k(y)}{i_k^{old}(y)}, \tag{19}$$

$$o_s^{new}(x) = \frac{o_s^{old}(x)}{K} \sum_{\forall k} \sum_{\forall y} \frac{h_k^{old}(y - x) d_k(y)}{i_k^{old}(y)}, \tag{20}$$

$$o_b^{new}(x) = \frac{o_b^{old}(x)}{K} \sum_{\forall k} \sum_{\forall y} \frac{h_k^{old}(y - x) d_k(y)}{i_k^{old}(y)}, \tag{21}$$

$$o^{new}(x) = \gamma^{new}\delta(x - x_p) + o_s^{new}(x) + o_b^{new}(x), \tag{22}$$

$$i_k^{new}(y) = \sum_{x \in X} h_k^{new}(y - x) o^{new}(x). \tag{23}$$

The PSF update equation remains the same as the baseline algorithm. The Gerchberg-Saxton phase retrieval algorithm is also applied after each PSF update equation, similar to the baseline algorithm.

2.2.2. System Integration

Since the new algorithm uses the estimates of the bright star and the PSFs from the baseline algorithm, it is integrated into the baseline as shown in Fig. 9. The same datasets used in the baseline algorithm are also used for the new algorithm.

2.2.3. Performance of Step 2

To compare the performance improvement of the new algorithm over the baseline algorithm, the same metrics described in Section 2.1.6 are also used. Using the new algorithm, all scenarios are processed with 1,000 EM iterations. For each EM iteration, 100 phase retrieval iterations are performed to recover the phase. For all scenarios, the neighborhood system function, $o_s(x)$, is made up of a 9×9 pixel plane centered on the bright star as shown in Fig. 10. The initial value for each pixel in the system function and that for the background function, $o_b(x)$, is assigned to 10 and 1 respectively for all scenarios.

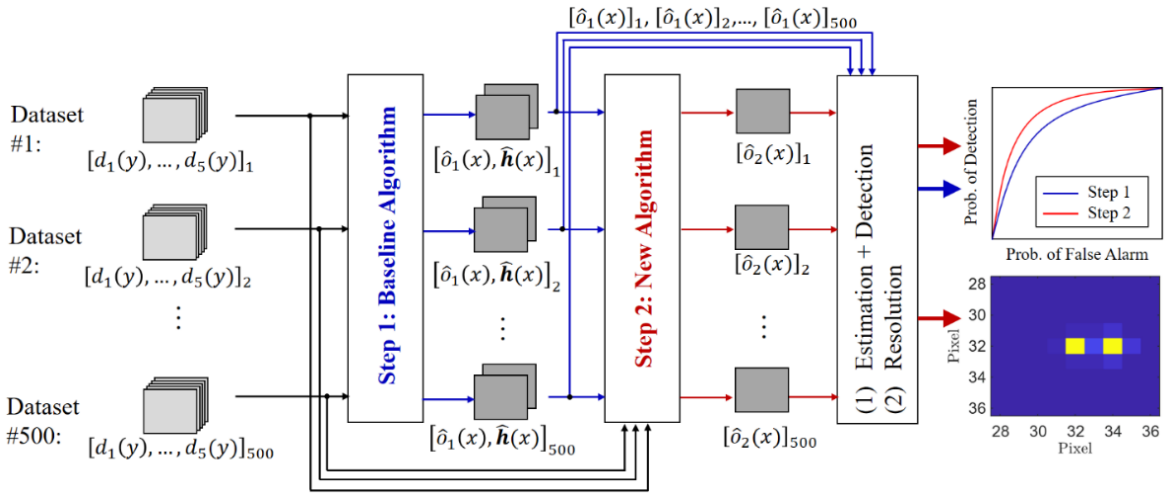

Fig. 9. System integration of the new algorithm with the baseline algorithm.

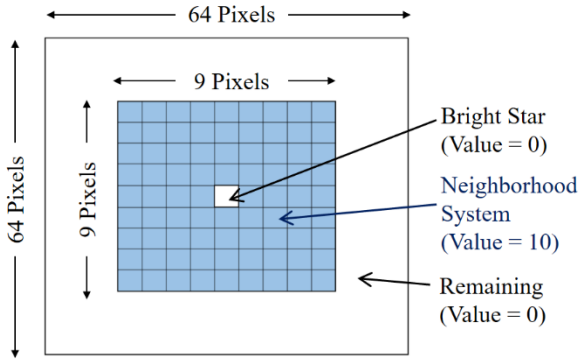

Fig. 10. The initial value for the neighborhood system function, $o_s(x)$, for all scenarios.

Similar to the baseline algorithm, the intensities of the dim star and that of the false alarm pixels are calculated using the same Gaussian mask function described in Equations (13) and (14). These intensities are also fitted to the gamma function. These gamma fits are used in generating the ROC functions. Figures 11 and 12 show the PDFs and the CDFs for the intensities of the dim star and that of the false alarm location for Scenarios 3 and 6 respectively, as the counterpart examples of Figures 5 and 6.

For the first performance metric, Fig. 13 compares the baseline algorithm (Step 1) with the new algorithm (Step 2) using the ROC functions for all scenarios. For all eight scenarios, the new algorithm outperforms the baseline algorithm.

For the second performance metric, Table 3 compares the intensity of the dim star with that of the middle pixel of the resolution function each scenario. From the results, Scenarios 1 through 6 are resolvable, where the intensities of the dim star are higher than that of the corresponding middle pixel. This is an improvement over the baseline algorithm, where Scenario 1 is the only resolvable case. Fig. 14 also shows the resolution functions for all scenarios.

In addition, Fig. 15 shows a set of recovered PSFs from the baseline algorithm and the new algorithm. A set of PSF was randomly chosen from one of the 500 datasets from one of the eight scenarios.

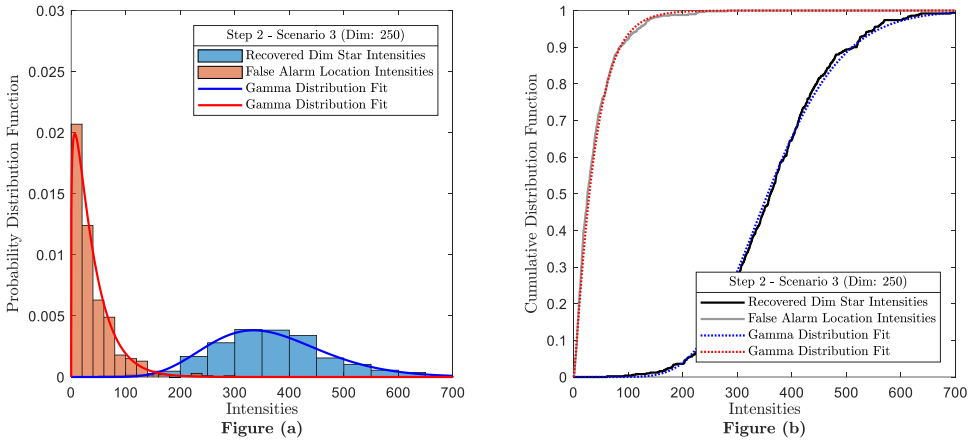

Fig. 11. The distributions of the intensities of the dim star and the false alarm pixel for Scenario 3.

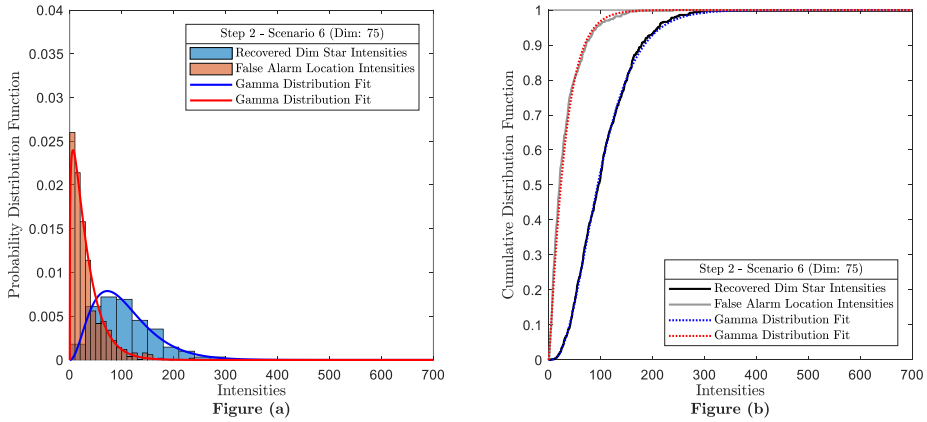

Fig. 12. The distributions of the intensities of the dim star and the false alarm pixel for Scenario 6.

Table 3. The comparison between the intensities of the dim star and the middle pixel of the resolution function for each scenario processed with the new algorithm.

Scenarios	Middle Pixel at (32, 33)	Dim Star at (32, 34)	Resolvable
Scenario 1	182	1525	Yes
Scenario 2	176	706	Yes
Scenario 3	139	324	Yes
Scenario 4	110	152	Yes
Scenario 5	100	117	Yes
Scenario 6	70	82	Yes
Scenario 7	58	56	No
Scenario 8	52	35	No

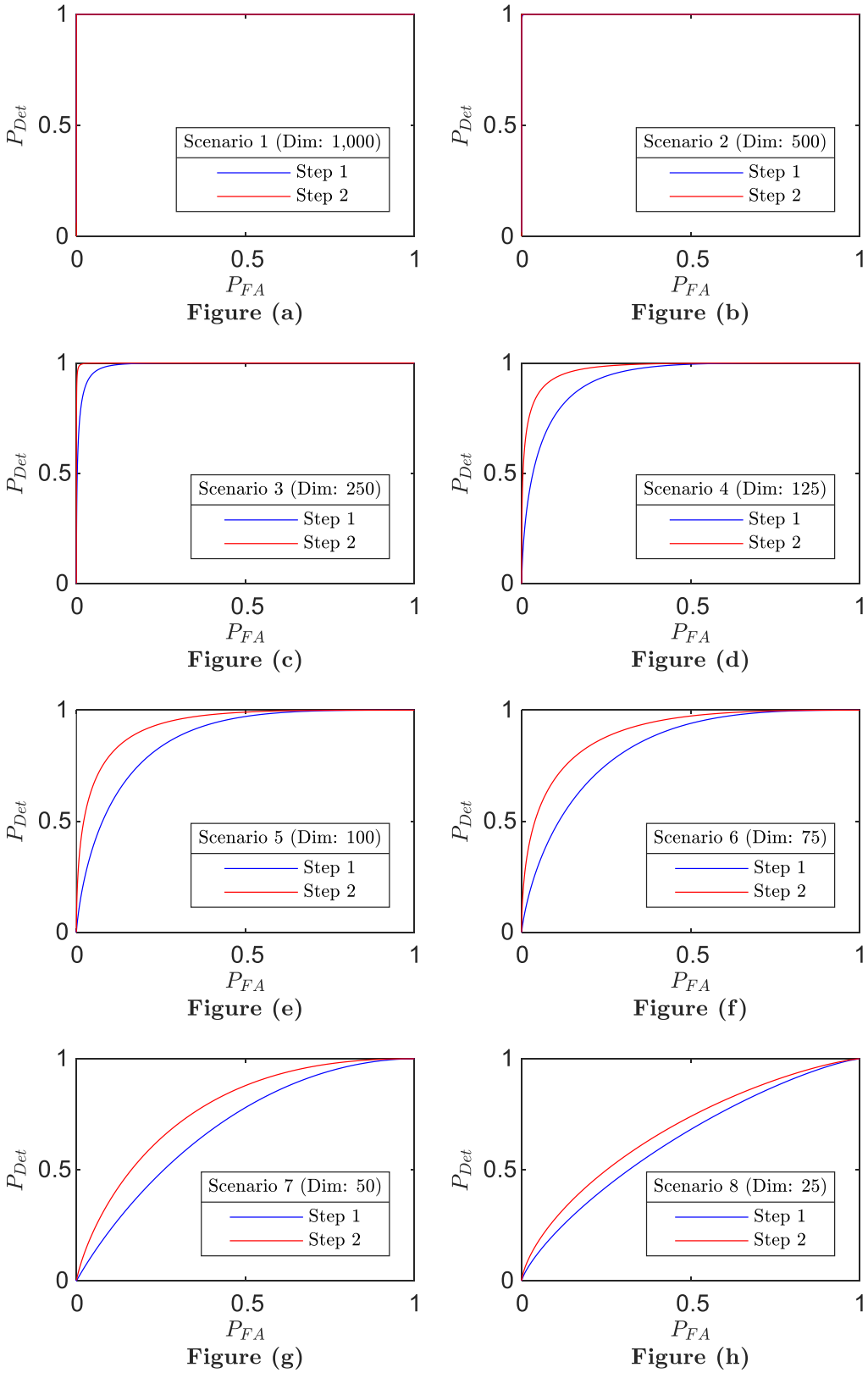

Fig. 13. The ROC functions compare the intensities of the dim star and that of the false alarm pixel for all scenarios which are processed with the baseline algorithm (Step 1) and the new algorithm (Step 2).

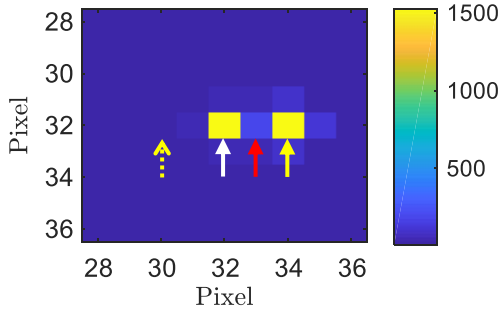

Fig. (a): Scenario 1 (Dim: 1,000)

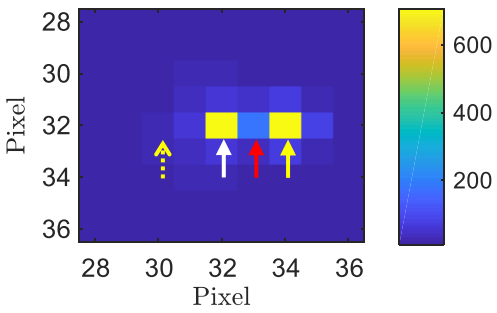

Fig. (b): Scenario 2 (Dim: 500)

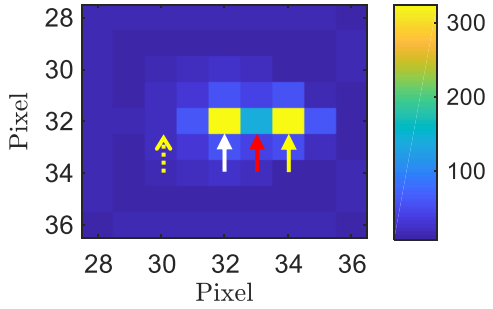

Fig. (c): Scenario 3 (Dim: 250)

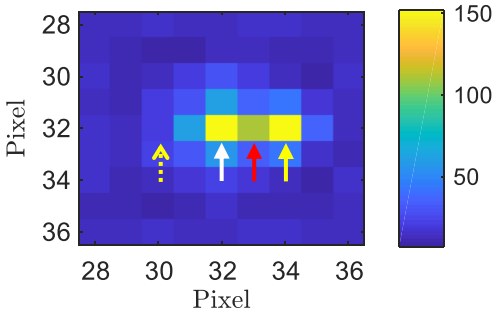

Fig. (d): Scenario 4 (Dim: 125)

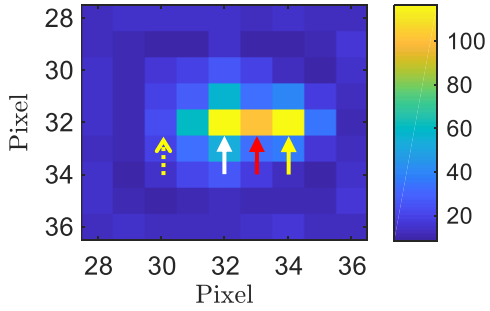

Fig. (e): Scenario 5 (Dim: 100)

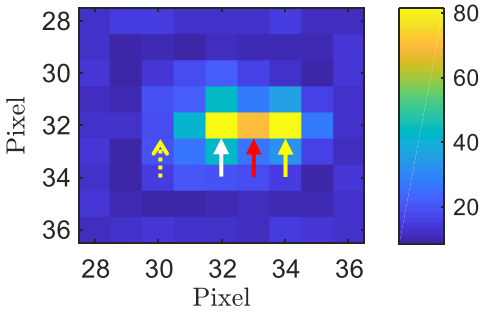

Fig. (f): Scenario 6 (Dim: 75)

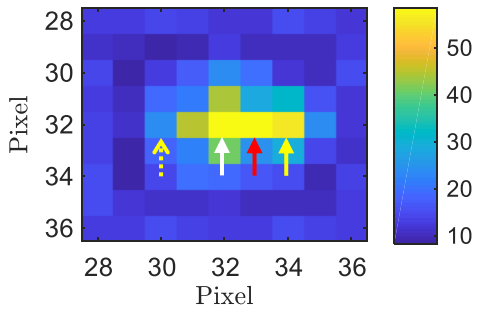

Fig. (g): Scenario 7 (Dim: 50)

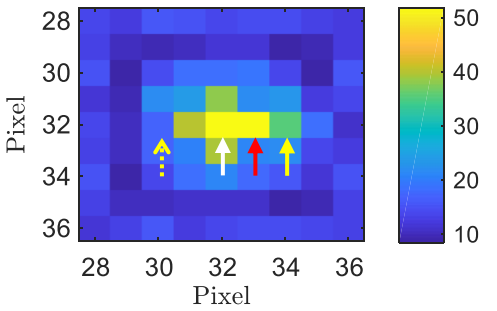

Fig. (h): Scenario 8 (Dim: 25)

Fig. 14. The resolution functions are calculated by averaging all 500 recovered object functions each scenario, using the new algorithm. The solid white, red, and yellow arrows indicate the bright star, the middle pixel, and the dim star respectively. The dotted yellow arrow indicates the false alarm pixel. The intensities of the middle pixel and the dim star are summarized in Table 3. Note: the intensities of the bright star are matched to the second brightest pixel to reduce the contrast ratio for all scenarios.

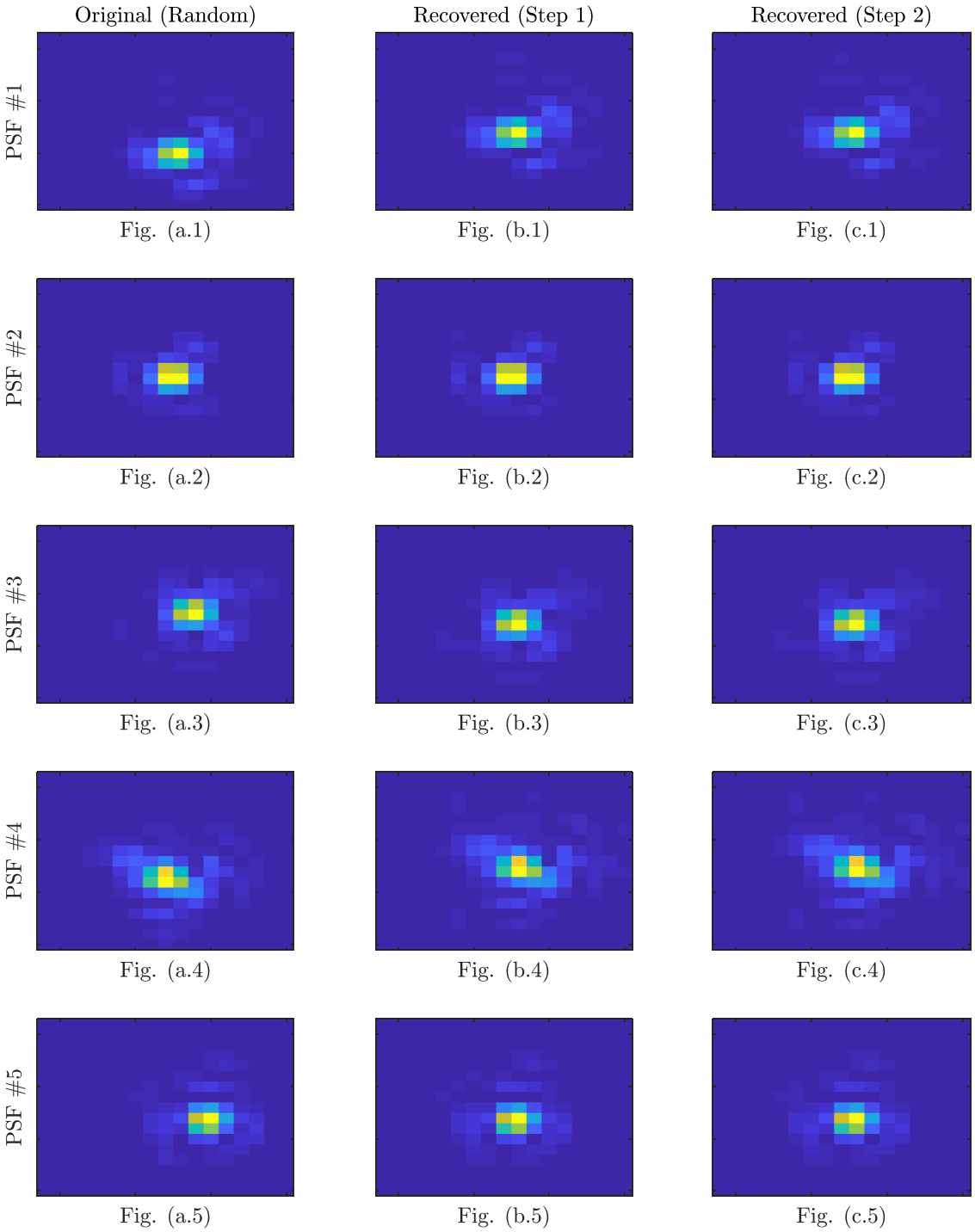

Fig. (a.1) Fig. (b.1) Fig. (c.1)

Fig. (a.2) Fig. (b.2) Fig. (c.2)

Fig. (a.3) Fig. (b.3) Fig. (c.3)

Fig. (a.4) Fig. (b.4) Fig. (c.4)

Fig. (a.5) Fig. (b.5) Fig. (c.5)

Fig. 15. A comparison of one set of five random atmospheric PSFs (first column) with the recovered PSF from the baseline algorithm (second column) and that from the new algorithm (third column). The set was randomly chosen from one of the 500 datasets from one of the eight scenarios.

3. LONG EXPOSURE IMAGING

In the long exposure case, the atmosphere has the opportunity to randomize many times during the detector integration process. This produces the sum of many short exposure PSFs where only one would be observed in images of point sources taken with short exposures. Attempting to accomplish phase retrieval of many phase screens for one observation poses a difficult task, therefore another approach is sought.

Supposing the integration time was large enough to allow many instances of atmospheric turbulence to produce PSFs that integrate long enough to mimic a long term average, then the impulse response of the system could be computed using the long exposure optical transfer function (OTF) computed by Fried [13]. The estimation of the seeing parameter would be the only task required in order to accomplish the PSF estimation step of a blind deconvolution algorithm and this has been addressed with some success in the past [14].

The more challenging task in the realm of long exposure imaging deals with the problem of long exposure images gathered by an optical system utilizing a closed loop control system which is partially compensating for some of the random Zernike modes presented to the telescope by the atmosphere. Although the PSF for this case has been computed analytically and can be computed using wave front sensor (WFS) data [15], the desire to allow the estimation of the PSF to adapt during the application of a blind deconvolution algorithm is still sought in some cases. This can be due to problems extracting the PSF from the WFS data or the possibility that the PSF is changing quickly compared to the time window used to compute the statistics necessary to characterized it. Despite its promise, problems with using the WFS data alone to compute the PSF remain and solutions are still sought for improving the quality of estimates obtained. One aspect of the PSF model for long exposure images taken with compensated systems is that the numbers of parameters are large, as all elements of the atmospheric Zernike coefficient correlation matrix first computed by Knoll are often sought.

The approach presented here simplifies the estimation problem by approximating the atmospheric PSF using only the diagonal of the atmospheric coefficient correlation matrix, thus reducing the number of variables to be estimated by the blind deconvolution algorithm. Equation (24) shows the form of the long exposure atmospheric transfer function [7]. In this section, the 2D coordinates are described with variable pairs.

$$H_L(f_x, f_y) = \frac{\mathrm{E}\left[\int_{-\infty}^{\infty}\int_{-\infty}^{\infty} A(u,v)e^{j\theta(u,v)}A(u-\lambda z f_x, v-\lambda z f_y)e^{-j\theta(u-\lambda z f_x, v-\lambda z f_y)}\partial u \partial v\right]}{\int_{-\infty}^{\infty}\int_{-\infty}^{\infty} A(u,v)A(u-\lambda z f_x, v-\lambda z f_y)\partial u \partial v}. \quad (24)$$

In this equation, H_L is the average transfer function, (f_x, f_y) are a spatial frequency pair in the horizontal and vertical directions of the image respectively, λ is the wavelength of the light, and z is the propagation distance from the entrance pupil to the CCD array. The phase, θ, is the atmospheric path delay of the light that enters the entrance pupil at position (u,v). This phase can be decomposed into Zernike polynomials as shown in Equation (3) [9].

We seek a simplified model for the PSF that maintains most of its fidelity while possessing a small number of parameters needed to define it. These competing goals can be addressed by observing that Noll's correlation matrix is nearly diagonal, thus only the diagonal terms of the correlation matrix, $C_{kk} = \mathrm{E}[(\alpha_k)^2]$, will be factored into the model, which leads to the simplified model for the phase structure function shown below [15]:

$$D_s(-\lambda z f_x, \lambda z f_y) = \mathrm{E}\left[\sum_{k=1}^{\infty} \alpha_k^2 (Z_k(u,v) - Z_k(u-\lambda z f_x, v-\lambda z f_y)^2\right]. \quad (25)$$

The blind deconvolution algorithm iteratively provides an estimate of the PSF, h^{EM}, which when operated on with a 2D Fourier transform yields the Fourier data, $H^{EM}(f_x, f_y)$ which is modeled as having a mean of:

$$\mathrm{E}\left[\mathcal{F}[h^{EM}(x,y)]\right] = \mathrm{E}\left[H^{EM}(f_x, f_y)\right] = H_L(f_x, f_y)\,. \tag{26}$$

The model coefficients, C_{kk}, are computed by minimizing the log-likelihood of the absolute value of $H_{EM,}$ treated as a Poisson random variable with a mean shown in Equation (26). Although the long exposure data is not likely Poisson distributed, this probability model captures the discrete and non-negative properties the amplitude of the estimated optical transfer function will have, since it is calculated from the Discrete Fourier Transform (DFT) of the estimated PSF. A value of one is added to the data and the mean in order to prevent numerical problems with taking the natural log of zero. The log-likelihood is summed over all spatial frequency components to provide the Q function, which must be minimized with respect to the model coefficients in order to estimate the PSF.

$$Q(C_{kk}) = \sum_{\forall f_x}\sum_{\forall f_y}\left[|H_{EM}(f_x, f_y)|+1\right]\ln\left(|H_L(f_x, f_y)|+1\right) - |H_L(f_x, f_y)| - 1\,. \tag{27}$$

Differentiating Q with respect to C_{oo}, setting that derivative equal to zero and subtracting the negative part of the derivative from both sides and then dividing both sides by it yields a ratio that is equal to one. When both sides are multiplied by the C_{oo} and old values of the parameters are utilized to compute the right side, the following iterative solution for the parameters is achieved:

$$C_{oo}^{new} = C_{oo}^{old}\,\frac{\sum_{\forall f_x}\sum_{\forall f_y}\frac{\left[|H_{EM}(f_x, f_y)|+1\right]}{\left[|H_L(f_x, f_y)|+1\right]}\frac{\partial|H_L(f_x, f_y)|}{\partial C_{oo}}}{\sum_{\forall f_x}\sum_{\forall f_y}\frac{\partial|H(f_x, f_y)|}{\partial C_{oo}}}\,. \tag{28}$$

This solution is pursued for all the coefficients compensated for by the adaptive optics system by setting k=o for all values of k between one and the maximum number of Zernike coefficients used to describe the atmospheric phase screen. For each iteration of the algorithm, $H_L(f_x, f_y)$ is computed by generating random realizations of atmospheric turbulence and using them to compute Equation (24). The random realizations for θ are generated via the following equation:

$$\theta(u,v) = \sum_{k=1}^{K}\sqrt{C_{kk}}\,n_k Z_k(u,v)\,, \tag{29}$$

where n_k are zero mean, unit variance Gaussian random variables and K is the maximum number of Zernike polynomials used to describe the atmospheric phase screens. A large number of random atmospheres are used to generate the average OTF described in Equation (24). The gradient of the OTF with respect to the elements of the Zernike coefficient covariance matrix is computed via:

$$\frac{\partial|H_L(f_x, f_y)|}{\partial C_{oo}} = \frac{|H_L(f_x, f_y)| - |H_\Delta(f_x, f_y)|}{\Delta}\,. \tag{30}$$

In this equation, Δ represents a change in the value of C_{oo} that is then used to generate H_Δ using the same process used to generate H_L. The iterations proceed until the change in the likelihood, Q, between iterations falls below a threshold of one.

This algorithm is intended for use on images captured with an adaptive optics system. It will be utilized in the future as this research endeavors to deal with cases where residual uncompensated aberrations make the discernment of a dim star near a bright one challenging.

4. SUMMARY

This paper presented techniques to overcome the image degradation due to the Earth's turbulent atmosphere using short exposure and long exposure methods. For short exposure imaging, a two-step iterative blind deconvolution algorithm was presented with the purpose of detecting and resolving a dim star in close proximity to a bright one. The first step was the expectation-maximization based iterative blind deconvolution algorithm proposed by Schulz with the Gerchberg-Saxton phase retrieval implementation. The estimates of the object function and the PSFs from the first step were further processed with the new algorithm in the second step, which was also based on the expectation-maximization algorithm. The two steps were compared using the two performance metrics, which were the ability to detect the dim star and the resolution between the dim star and the bright star. From the results shown, the new algorithm outperformed the baseline algorithm in both performance metrics. This paper also provided a mathematical model for estimating the long exposure PSF for adaptive optics system for future research.

5. ACKNOWLEDGEMENTS

This work was sponsored by the Air Force Office of Scientific Research under MIPR F4FGA09014J00318. The opinions and views expressed by the authors do not necessarily reflect those of the United States Air Force or the Department of Defense.

6. REFERENCES

[1] R. D. Richmond and S. C. Cain, *Direct-Detection LADAR Systems*. 2010.
[2] S. M. Jefferies and J. C. Christou, "Restoration of Astronomical Images by Iterative Blind Deconvolution," *Astrophys. J. v.415, p.862*, vol. 415, p. 862, Oct. 1993.
[3] T. J. Schulz, "Multiframe Blind Deconvolution of Astronomical Images," *J. Opt. Soc. Am.*, vol. 10, no. 5, p. 1064, 1993.
[4] J. W. Goodman, *Statistical Optics*. New York: John Wiley & Sons, 2000.
[5] R. W. Gerchberg and W. O. Saxton, "A Practical Algorithm for the Determination of the Phase from Image and Diffraction Plane Pictures," *Optik (Stuttg).*, vol. 35, pp. 237–246, 1972.
[6] A. P. Dempster, N. M. Laird, and D. B. Rubin, *Maximum Likelihood from Incomplete Data via the EM Algorithm*, vol. 39, no. 1. 1977.
[7] J. W. Goodman, *Introduction to Fourier Optics*, 3rd ed. Greenwood Village: Roberts & Company Publishers, 2005.
[8] R. J. Noll, "Zernike Polynomials and Atmospheric Turbulence," *J. Opt. Soc. Am.*, vol. 66, no. 3, pp. 207–211, 1976.
[9] N. A. Roddier, "Atmospheric Wavefront Simulation Using Zernike Polynomials," *Opt. Eng.*, vol. 29, no. 10, pp. 1174–1180, Oct. 1990.
[10] I. B. Putnam and S. C. Cain, "Modeling a Temporally Evolving Atmosphere with Zernike Polynomials," *Advanced Maui Optical and Space Surveillance Technologies Conference*, 2012. [Online]. Available: https://amostech.com/TechnicalPapers/2012/Adaptive_Optics_Imaging/PUTNAM.pdf. [Accessed: 01-May-2019].
[11] G. J. Hahn and S. S. Shapiro, *Statistical Models in Engineering*. New York: John Wiley & Sons, 1967.
[12] S. C. Cain, "Super-Resolution Imaging via Expectation-Maximization Estimation of Near Stellar Neighborhoods," in *Proc. SPIE*, 2018, vol. 10772.
[13] D. L. Fried, "Limiting Resolution Looking Down Through the Atmosphere," *J. Opt. Soc. Am.*, vol. 56, no. 10, pp. 1380–1384, 1966.
[14] A. MacDonald and S. C. Cain, "Parameterized Blind Deconvolution of Laser Radar Imagery Using an Anisoplanatic Optical Transfer Function," *Opt. Eng.*, vol. 45, no. 11, pp. 1–12, Nov. 2006.
[15] J.-P. Véran, F. Rigaut, H. Maître, and D. Rouan, "Estimation of the Adaptive Optics Long-Exposure Point-Spread Function Using Control Loop Data," *J. Opt. Soc. Am. A*, vol. 14, no. 11, pp. 3057–3069, 1997.